

Observed and Modeled Warm Rainfall Occurrence and Its Relationships with Cloud Macrophysical Properties

JOSHUA M. KING,* CHRISTIAN D. KUMMEROW, SUSAN C. VAN DEN HEEVER, AND MATTHEW R. IGEL

Department of Atmospheric Science, Colorado State University, Fort Collins, Colorado

(Manuscript received 8 December 2014, in final form 20 July 2015)

ABSTRACT

Observed and modeled rainfall occurrence from shallow (warm) maritime clouds and their composite statistical relationships with cloud macrophysical properties are analyzed and directly compared. Rain falls from ~25% of warm, single-layered, maritime clouds observed by *CloudSat* and from ~27% of the analogous warm clouds simulated within a large-domain, fine-resolution radiative–convective equilibrium experiment performed using the Regional Atmospheric Modeling System (RAMS), with its sophisticated bin-emulating bulk microphysical scheme. While the fractional occurrence of observed and simulated warm rainfall is found to increase with both increasing column-integrated liquid water and cloud depth, calculations of rainfall occurrence as a joint function of these two macrophysical quantities suggest that the modeled bulk cloud-to-rainwater conversion process is more efficient than observations indicate—in agreement with previous research. Unexpectedly and in opposition to the model-derived relationship, deeper *CloudSat*-observed warm clouds with little column water mass are more likely to rain than their corresponding shallow counterparts, despite having lower cloud-mean water contents. Given that these composite relationships were derived from statically identified warm clouds, an attempt is made to quantitatively explore rainfall occurrence within the context of the warm cloud life cycle. Extending a previously established cloud-top buoyancy analysis technique, it is shown that rainfall likelihoods from positively buoyant RAMS-simulated clouds more closely resemble the surprising observed relationships than do those derived from negatively buoyant simulated clouds. This suggests that relative to the depiction of warm clouds within the RAMS output, *CloudSat* observes higher proportions of positively buoyant, developing warm clouds.

1. Introduction

Low-level, liquid-phase (warm) clouds cover vast portions of the global oceans (e.g., Mace et al. 2007; Medeiros et al. 2010) and play a critical role in the global energy balance (e.g., Hartmann et al. 1992). Varying in form from temporally persistent stratocumulus decks only a few hundred meters thick to transient trade wind cumulus clouds with depths approaching 3–4 km, these clouds are commonly found in regions characterized by large-scale atmospheric subsidence. The simulation of marine boundary layer clouds represents a large source of uncertainty for estimates of climate sensitivity (e.g.,

Bony and Dufresne 2005; Webb et al. 2006). Uncertainties in the parameterized microphysical processes active within these clouds lead to a global climate model depiction of rainfall that is generally too frequent and too light (Stephens et al. 2010).

Rain from warm, maritime clouds is typically not as heavy as that which falls from deeper convection (rates of less than a few millimeters per hour; e.g., Lebsock and L'Ecuyer 2011; Berg et al. 2010). However, it is ubiquitous and, thus, contributes nonnegligibly to the total amount of precipitation that falls over the globe. Active satellite remote sensors have been used to estimate that warm rainfall accounts for ~20% of the total rain that falls over the oceans (Short and Nakamura 2000; Lau and Wu 2003; Liu and Zipser 2009; Chen et al. 2011).

While early observational studies concluded that rainfall from warm, maritime clouds was common (e.g., Byers and Hall 1955), more recent analyses have utilized both surface- and satellite-based observations to quantify the fractional occurrence of rainfall from this cloud type. Based on data collected during the Rain in

* Cooperative Institute for Mesoscale Meteorological Studies, University of Oklahoma, Norman, Oklahoma.

Corresponding author address: Joshua King, Cooperative Institute for Mesoscale Meteorological Studies, University of Oklahoma, 120 David L. Boren Blvd., Norman, OK 73072.
E-mail: jking@ou.edu

Cumulus over the Ocean (RICO; Rauber et al. 2007) field campaign in the western tropical North Atlantic, it was estimated that $\sim 10\%$ of the observed shallow cloud distribution produced rain (Nuijens et al. 2009; Snodgrass et al. 2009). Given its global coverage and unique sensitivity to both cloud droplet hydrometeors and light rainfall, many recent studies have employed *CloudSat* (Stephens et al. 2002)—the sensor utilized in the present study—to estimate the frequency of occurrence of rainfall from warm clouds over the oceans (Haynes and Stephens 2007; Lebsock et al. 2008; Leon et al. 2008; Kubar et al. 2009; Chen et al. 2011; Suzuki et al. 2011; Rapp et al. 2013; Christensen et al. 2013). Using a profile-maximum *CloudSat* reflectivity drizzle threshold, Kubar et al. (2009) estimated that up to 80% of the identified warm clouds over the central Pacific Ocean contained drizzle or rain hydrometeors at some vertical level. Taking a more conservative approach, Lebsock et al. (2008) used near-surface *CloudSat* reflectivity to identify rainfall incidence and accounted for warm clouds undetected by *CloudSat* (cloud tops obscured by surface contamination and/or low reflectivities), but observed by the Moderate Resolution Imaging Spectroradiometer (MODIS), to estimate that only 6.5% of warm clouds over the global oceans certainly produced rainfall adjacent to the surface. The rainfall occurrence differences between these latter two highlighted observational studies point to a need for defining rainfall in a consistent manner, especially if models are to be evaluated against observations.

Examining how the frequency of occurrence of rainfall from these warm clouds is related to cloud macrophysical properties—the large-scale characteristics of the clouds themselves—can provide insight into the factors affecting the warm rain processes active within this cloud type. Observational evidence from both ground-based sensors (Zuidema et al. 2005; Rémillard et al. 2012) and spaceborne sensors (Lebsock et al. 2008; Leon et al. 2008; Kubar et al. 2009; L'Ecuyer et al. 2009; Chen et al. 2011; Suzuki et al. 2011; Christensen et al. 2013) has indicated that warm clouds with higher cloud liquid water paths—the vertically integrated liquid water mass within the cloud column—are more likely to produce drizzle and rain. This suggests that warm clouds are most likely to develop precipitation when greater amounts of cloud water are available for warm rain processes. A strong link has also been observed between cloud depth and warm rain production (Byers and Hall 1955; Nuijens et al. 2009; Stephens et al. 2008a; Kubar et al. 2009; Snodgrass et al. 2009; Reiche and Lasher-Trapp 2010; Rémillard et al. 2012; Christensen et al. 2013). The physical reason for the existence of the latter relationship remains less clear but could be related to

such key, and potentially interrelated, factors as liquid water availability and relative cloud age (e.g., Reiche and Lasher-Trapp 2010).

Warm rain collision and coalescence processes within cloud-resolving models and larger-scale climate models are commonly parameterized through empirically derived cloud-to-rain conversion rates (e.g., Kessler 1969; Manton and Cotton 1977). To assess relative model skill at representing warm rain formation processes, Suzuki et al. (2011) compared warm rain statistics observed over the global oceans by *CloudSat* and MODIS to those simulated with regional and global cloud-resolving models. Regional simulation output analyzed in that study was from a large-domain, high-resolution radiative-convective equilibrium (RCE) experiment performed with the Regional Atmospheric Modeling System (RAMS; Cotton et al. 2003; Saleeby and van den Heever 2013) using two-moment, bin-emulating microphysics, while global model output was obtained from a simulation performed using a simpler, single-moment Kessler-type microphysical scheme within the Non-hydrostatic Icosahedral Atmospheric Model (NICAM; Tomita and Satoh 2004; Satoh et al. 2008). It was shown that for the same liquid water path, both models produced drizzle and rain more readily than observations suggested. However, RAMS and its more sophisticated microphysical scheme significantly outperformed NICAM in its depiction of the efficiency with which cloud water was converted to drizzle and rainwater. Given the realistic representation of warm rain processes in RAMS, this study now further analyzes the characteristics of warm rain simulated using this model.

Composite rainfall statistics derived from instantaneous snapshots of clouds that are in various stages of growth, maturity, and dissipation inherently reflect the amount of time the clouds spend within these life cycle stages. However, as clouds develop and mature in time, it is likely that their associated macrophysical properties (e.g., geometric depth and liquid water path) evolve prior to the onset of rainfall (e.g., Reiche and Lasher-Trapp 2010; Burnet and Brenguier 2010; Witte et al. 2014). In an effort to more accurately characterize instantaneous *CloudSat* observations of identified cumulus congestus clouds, Luo et al. (2009) developed a methodology that provided a dynamic context for snapshot observations of this deep convective cloud type. The concept was based upon assessing whether the tops of clouds were, at the time of observation, positively or negatively buoyant relative to their surrounding environment. Positively buoyant (transient) clouds, those with cloud-top temperatures warmer than the environmental temperature at the same height, were interpreted to have been actively growing when

observed; negatively buoyant (terminal) clouds were more likely to have already ceased their vertical development. While Luo et al. (2009) did not investigate rainfall or shallow clouds within their terminal–transient framework, an attempt is made within this study to apply a similar analysis technique to quantitatively explore warm rainfall occurrence within the context of cloud life cycle.

The principal aim of this study is to compare composite statistical relationships between warm rainfall occurrence and cloud macrophysical properties observed by *CloudSat* to those simulated with RAMS. To this end, the research presented herein aims to address the three following questions:

- 1) What percentage of *CloudSat*-observed warm clouds produce rainfall over the global oceans, and how does this frequency compare to that simulated with RAMS?
- 2) How is warm rainfall occurrence statistically related to two key macrophysical parameters—column-integrated water mass and cloud depth—and what do these relationships imply about rainfall production within these warm clouds?
- 3) What insight, if any, do these warm rainfall occurrence statistics provide on the nature of the life cycle of clouds within these distributions?

To address these questions, a methodology designed to identify and compare *CloudSat*-observed and RAMS-simulated warm, single-layered clouds in a consistent manner is outlined within section 2. Warm rainfall occurrence statistics and their composite relationships with cloud macrophysical properties for this warm cloud subset are presented within section 3. Based on these results, the influence of warm cloud life cycle on these rainfall occurrence statistics is examined within section 4.

2. Data and methods

a. *CloudSat* observations

The observational datasets used throughout this study were derived from *CloudSat* (Stephens et al. 2002), a mission that flies a nadir-pointing 94-GHz (W band) cloud profiling radar (CPR; Im et al. 2005). The CPR has approximate footprint dimensions of 1.7 km × 1.4 km (along and cross track, respectively) and a pulse length–determined vertical resolution of 480 m that is oversampled to 240 m. With a minimum detectable signal of approximately −30 dBZ, the CPR is a well-suited instrument to observe clouds and their transition to producing precipitation. All *CloudSat* results presented within this study have been derived from an ocean-only data record extending from July 2006 to April 2011 (~4.75 yr).

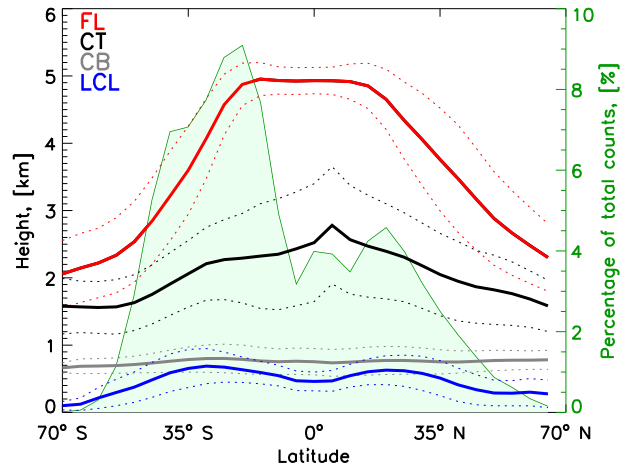


FIG. 1. Zonally averaged freezing-level height (red), cloud-echo-top height (black), cloud-echo-base height (gray), and lifting condensation level (blue) for *CloudSat*-observed warm, single-layered clouds. Thick lines represent the zonal mean, and dotted lines represent the zonal standard deviation about the zonal mean. The underlying green curve represents the percentage contribution of cloud counts from each zonal band to the total number of observed clouds. For Figs. 1 and 2, native-resolution *CloudSat* data were gridded to a 5° lat × 5° lon resolution.

Observed cloud vertical extent properties were obtained from the *CloudSat* geometrical profiling product (2B-GEOPROF) cloud mask (Marchand et al. 2008). Generally, as 2B-GEOPROF cloud mask values increase from 10 (very weak echo) to a maximum of 40 (strong echo), the percentage of possible false hydrometeor detections decreases from <50% to <0.2%. For this study, cloudy range bins within the *CloudSat* profiles were defined as those with a 2B-GEOPROF cloud mask value ≥ 20 , a threshold that removed likely surface clutter from the analysis and ensured that the percentage of false hydrometeor detection was $\sim 5\%$ (Marchand et al. 2008). Utilizing this definition, vertically contiguous cloudy *CloudSat* range bins, and the heights of these range bins, were used to determine cloud-echo-top and -base heights for cloud layers within the observed profiles. To directly examine the relationships between liquid-phase cloud geometric characteristics and cloud column-integrated properties, the analysis was restricted to profiles containing single cloud layers with echo-top heights at or below the scene's freezing-level height—a field calculated from ancillary temperature profile information from the *CloudSat* European Centre for Medium-Range Weather Forecasts (ECMWF) auxiliary data product (ECMWF-AUX). As very few warm clouds were detected at high latitudes, the analysis was limited to scenes observed equatorward of 70°N and 70°S.

The resulting database contained 20.5 million *CloudSat* observations of warm, single-layered clouds. The zonal-mean

vertical extent characteristics of this core dataset (Fig. 1) indicate that the zonal-mean cloud-echo-top heights (CT; black) mirror the latitudinal variation in freezing-level height (FL; red), with a maximum near the equator and minima at the poleward latitude extrema considered in this analysis. The zonal consistency in the identified cloud-echo-base heights (CB; gray) may in part be related to either surface clutter limiting *CloudSat*'s ability to detect cloud bases located within the three lowest vertical range gates (below ~ 720 m) or to rainfall obscuring actual cloud bases in precipitating scenes. However, the mean lifting condensation level (LCL; blue) calculated for this cloud distribution from ancillary ECMWF-AUX temperature and specific humidity fields was 570 m, a mere 200 m (or, the approximate depth of a single *CloudSat* vertical range gate) lower than the mean identified cloud-echo-base height of 770 m. This result lends some credibility to the cloud-echo-base heights summarized in Fig. 1.

Delineation of raining and nonraining clouds was achieved through the use of the *CloudSat* 2C-PRECIP-COLUMN precipitation incidence flag (Haynes et al. 2009). For this study, raining scenes were defined as those flagged as rain certain, indicating that the unattenuated near-surface (~ 600 – 840 m) reflectivity Z_u exceeded 0 dB. Scenes with either no rain ($Z_u < -15$ dB), rain possible ($-15 < Z_u < -7.5$ dB), or rain probable ($-7.5 < Z_u < 0$ dB) flags were classified as nonraining. By conservatively defining raining *CloudSat* scenes as those flagged as rain certain, the rainfall detection uncertainty herein is likely considerably lower than the 20%–25% estimate put forth by Stephens et al. (2010), where both rain certain and rain probable flags were used to demarcate rainfall. Count maps of the resulting nonraining and raining warm cloud distributions (Figs. 2a,b, respectively) indicate that while most tropical and subtropical oceanic regions were well represented (≥ 1000 total counts), the greatest density of raining and nonraining clouds were identified over the prominent subtropical stratocumulus regions (e.g., Wood 2012).

To quantify the fractional occurrence of warm rainfall for these clouds, a simple rain fraction was calculated by dividing the raining cloud counts by the total (raining plus nonraining) cloud counts. While the overall resulting rain fraction for the *CloudSat*-observed cloud distribution was 25.4%, clear regional variability in the relative occurrence of warm rainfall does exist (Fig. 2c). This *CloudSat*-only overall fractional occurrence exceeds the A-Train-derived estimate of 6.5% put forth by Lebsock et al. (2008), a result that is likely related to the nonraining classification Lebsock et al. (2008) assigned to warm, oceanic clouds missed by *CloudSat* but detected by MODIS.

The *CloudSat* 2C-PRECIP-COLUMN product also provided an estimate of the two-way, path-integrated

attenuation of the CPR beam due to hydrometeors (hereafter PIA; Haynes et al. 2009). This field is related to the column-integrated total water path and is explored in detail within section 3a.

b. Mesoscale model simulations

Mesoscale model output for this study was simulated with RAMS (Cotton et al. 2003; Saleeby and van den Heever 2013). Conceived and refined at Colorado State University, RAMS is a nonhydrostatic, regional cloud-resolving model. The bin-emulating, bulk cloud microphysical scheme operating within RAMS makes use of lookup tables precalculated from a detailed bin-resolving model to simulate the rate of change in cloud and rain mixing ratios and number concentrations due to collision and coalescence processes (Feingold et al. 1998; Saleeby and Cotton 2004).

To adequately evaluate the characterization of rainfall from warm clouds within RAMS and to compare this representation to *CloudSat* observations, a large, RAMS-derived statistical sample was needed at a spatial resolution comparable to that of *CloudSat*. Output from a large-domain (6×10^5 km²), high-resolution (1-km horizontal grid spacing with 32 model layers below an altitude of 5 km) RAMS RCE experiment described by Igel et al. (2015) was used for this purpose. Pertinent characteristics of the model setup are summarized in Table 1. Initialized from a sounding characteristic of the mean tropical atmosphere, the simulation utilized a two-moment, bin-emulating bulk microphysical scheme, a horizontally and vertically homogeneous aerosol concentration of 100 cc^{-1} , and was run for 70 days, reaching a state of RCE at day 30. A number of simulations operating under conditions of RCE have previously been used to successfully study the characteristics of tropical clouds (e.g., Stephens et al. 2008b; van den Heever et al. 2011; Storer and van den Heever 2013). In this study, hourly RAMS output from the final 3 weeks of the simulation was analyzed.

To facilitate direct comparisons with *CloudSat* observations, all model data were processed with the QuickBeam radar simulator (Haynes et al. 2007), which was developed for this express purpose. Using a specified frequency of 94 GHz to mimic the CPR, QuickBeam-simulated profiles of reflectivity and column PIA values from RAMS were available for comparison with those from *CloudSat* following processing. To define consistent cloud boundaries for the RAMS dataset, the relationship between the 2B-GEOPROF cloud mask values and observed CPR reflectivities at all altitudes was investigated for January and July 2007. The mean reflectivities associated with the cloud mask value of 20 used to define cloud boundaries in

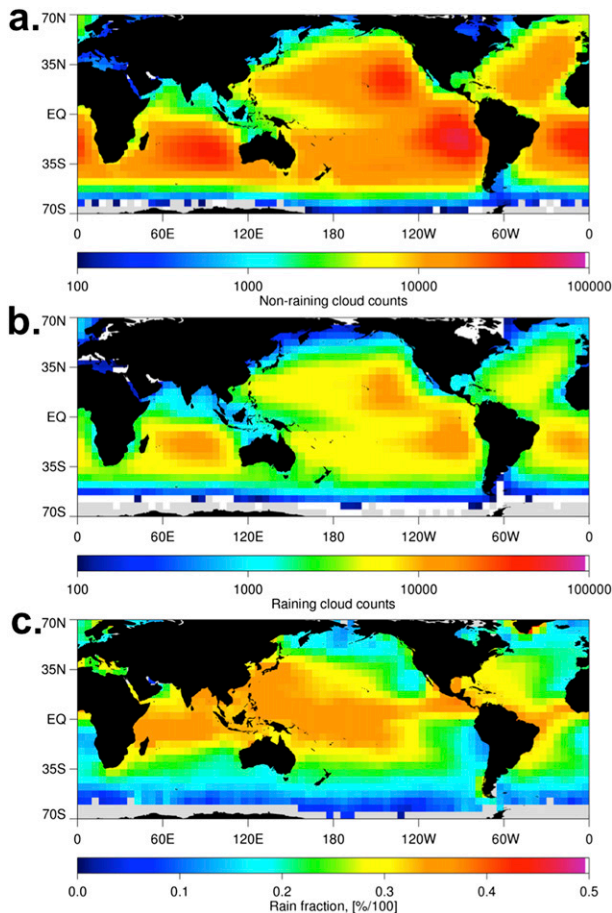


FIG. 2. Maps of (a) nonraining and (b) raining warm, single-layered cloud counts. (c) Map of the fraction of raining counts to total (raining and nonraining) counts in each grid box. In (a) and (b), grid boxes without any cloud counts are colored gray. In (c), grid boxes with fewer than 100 total cloud counts are colored gray.

the *CloudSat* portion of this analysis were -26.0 and -25.8 dBZ for January and July 2007, respectively. Based on these results, a reflectivity value of -26 dBZ was used to define cloudy portions of the RAMS domains. Accordingly, the cloud-base (top) height for a given cloud layer was defined as the lowest (highest) model-level height within a vertically contiguous block of model grid points whose simulated reflectivities exceeded this threshold value. After screening for RAMS grid boxes that contained a single cloud layer with a top height at or below the freezing-level height, a total of 71.6 million RAMS warm, single-layered cloudy scenes were identified. To ensure sound comparisons with output from this tropical RCE simulation, a number of additional observational subsetting experiments were applied to the full *CloudSat* dataset; they are discussed in section 3c.

Utilizing reflectivity output from QuickBeam, raining and nonraining clouds were delineated by applying the

same Z_u threshold classifications outlined in section 2a. The overall rain fraction for the RAMS-simulated warm cloud distribution was 27.4%—a value that compares very well with the corresponding *CloudSat*-identified rain fraction of 25.4%.

3. Observed and modeled warm rainfall occurrence

a. Dependence on column-integrated liquid water

Motivated by the desire to better understand the bulk conversion of cloud water to rainwater within the cloud column, it was of interest to first investigate the relationship between column-integrated water mass and the occurrence of *CloudSat*-observed and RAMS-simulated warm rainfall. To this end, an approximately linear mean relationship was found between total liquid water path [TWP; sum of cloud water path (CWP), drizzle water path (DWP), and rainwater path (RWP)] and QuickBeam-simulated 94-GHz PIA values for the RAMS warm cloud distribution (Fig. 3). Given this relationship and the fact that PIA was a common field between the processed model output and the *CloudSat* observations, PIA was used as a proxy for column-integrated water mass for these warm clouds.

The fractional occurrence of warm rainfall within the *CloudSat*-observed and RAMS-simulated warm cloud distributions is shown as a function of PIA percentiles at a 5% step in Fig. 4. Rainfall likelihoods within both datasets increased nearly monotonically as a function of increasing PIA, in line with previously described direct relationships between column-integrated water mass and the occurrence of warm rainfall (Lebsack et al. 2008; L'Ecuyer et al. 2009; Kubar et al. 2009; Suzuki et al. 2011).

CloudSat-observed warm rain was more likely than not (50% fractional occurrence; green dashed line in Fig. 4) at a PIA value of ~ 3 dB, which corresponds to an equivalent RAMS-derived TWP value of 325 gm^{-2} (Fig. 3). Within RAMS, this same warm rainfall occurrence threshold was eclipsed at a PIA value of ~ 2 dB (TWP of $\sim 225 \text{ gm}^{-2}$). This indicates that RAMS-simulated warm clouds produced rainfall more frequently at lower PIA values than their observed counterparts—in line with the findings of Suzuki et al. (2011) and suggesting that the conversion of cloud to rainwater occurs more readily within the model than is observed in nature.

The percentile portion of the analysis in Fig. 4 reveals that the *CloudSat* distribution of PIA for these warm clouds extended to higher values than were simulated with RAMS. The median PIA value of the 95th–100th *CloudSat* PIA percentile bin was more than twice as large as that from RAMS (11.6 and 5.3 dB, respectively).

TABLE 1. RAMS RCE simulation characteristics. This simulation is referred to as DM_A100 within Igel et al. (2015).

Horizontal domain	3000 × 200 grid points; 1-km grid spacing
Vertical domain	65 grid points; 25-km domain top altitude; 70-m surface grid spacing stretched to 750 m aloft
Microphysical scheme	Two-moment, bin-emulating bulk scheme
Hydrometeor species	Eight in total: cloud, drizzle, rain, pristine ice, snow, aggregates, graupel, and hail
SST	Fixed at 300 K
Incoming solar radiation	Fixed at 450 W m ⁻²
Aerosol	Fixed (horizontally and vertically) at 100 cc ⁻¹

If rain removes water mass from the atmospheric column, a more efficient production of rain within RAMS may have acted to limit the maximum attainable PIA within the modeled cloud distribution.

b. Relationship with cloud depth

This section explores the relationship between warm rainfall occurrence and cloud depth. To ensure that the warm clouds analyzed within this and subsequent sections were rooted within the boundary layer (i.e., not high-based fragments of cloud situated below the freezing level), the analysis was further restricted to *CloudSat*-observed and RAMS-simulated warm, single-layered clouds with cloud-echo-base heights identified at or below 1000 m AGL. While it is possible that surface contamination of the *CloudSat* radar beam could effectively mask actual cloud bases residing below this altitude, the surface sets the absolute limit for any additional cloud depth that was effectively unidentified through this methodology. While this screening step reduced the total number of *CloudSat* (RAMS) clouds analyzed to 18.1 million (70.8 million), the overall *CloudSat* (RAMS) rain fraction increased by 3.3%–28.7% (0.3%–27.7%). These constrained datasets form the basis for the results presented throughout the remainder of this study.

In composite, *CloudSat*-observed and RAMS-simulated warm rainfall likelihoods increased with increasing deciles of cloud depth (Fig. 5). These results are qualitatively consistent with the observationally based relationship described by Byers and Hall (1955) and nearly quantitatively identical to those derived from a limited amount of early (2006/07) *CloudSat* data presented by Stephens et al. (2008a), suggesting that these relationships are robust. The notable exception to the general cloud depth–rain fraction relationship agreement between *CloudSat* and RAMS is found at cloud depths of ~2 km, where simulated clouds were up to 20% less likely to rain than their observed counterparts.

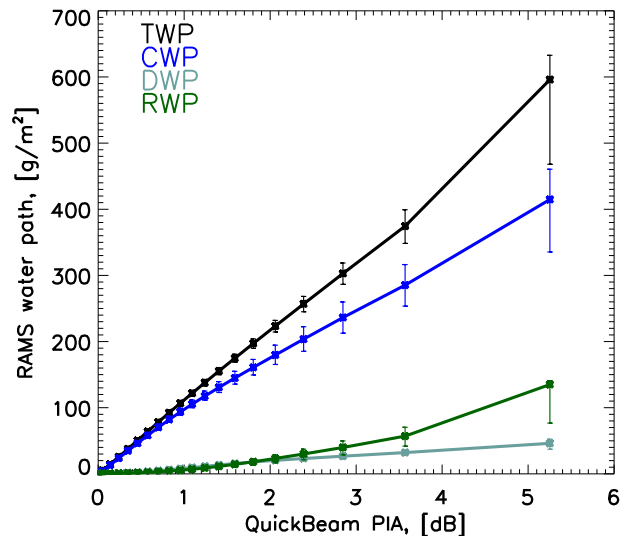


FIG. 3. RAMS water path values as a function of percentiles of corresponding QuickBeam-simulated 94-GHz PIA at a 5% step for the warm cloud subset. Thick points represent the mean water path value in each PIA percentile bin. Lower and upper bars represent the 25th and 75th water path percentiles in each PIA percentile bin, respectively. TWP (black) is the sum of CWP (blue), DWP (light green), and RWP (dark green).

This result could be related to factors such as atmospheric thermodynamic structure or entrainment that are outside of the scope of the macrophysical focus of this study.

As the cloud attribute of depth in itself was not expected to actively promote warm rainfall production, it was of interest to determine the physical mechanism or mechanisms responsible for this robust relationship. In section 3a, it was shown that observed and simulated warm clouds were more likely to rain as column-integrated water mass increased (Fig. 4). In turn, column-integrated water mass is known to be directly related to cloud depth. In adiabatic conceptualizations of shallow clouds, wherein cloud liquid water content increases linearly with height above cloud base, adiabatic cloud liquid water path is proportional to the square of cloud depth (e.g., Albrecht et al. 1990; Pawlowska and Brenguier 2003).

The thick mean curves in Fig. 6 show that PIA increased as a function of deciles of cloud depth for both observed and simulated warm clouds. This indicates that in the mean, deeper warm clouds contained more and/or larger liquid hydrometeors that acted to collectively attenuate the real and simulated 94-GHz radar beam to a greater degree. These results collectively imply that the increased availability of liquid water within deeper clouds preferentially promoted the production of their rainfall through warm rain processes—consistent with the conclusions of Reiche and Lasher-Trapp (2010).

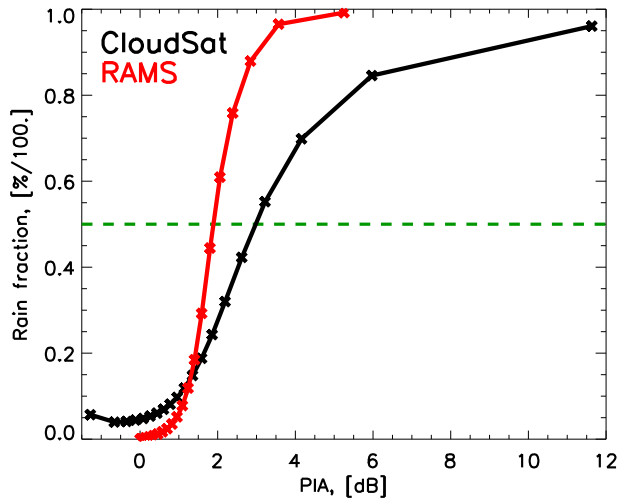


FIG. 4. Rain fraction as a function of percentiles of PIA at a 5% step for *CloudSat* (black) and RAMS (red) warm clouds. Nodes represent the median PIA value within each PIA percentile bin. In this and subsequent figures, the dashed green line is plotted at a constant fractional occurrence of 50% to indicate where rainfall is more likely than not.

Another plausible physical link between cloud depth and rainfall occurrence could simply be *time*. Developing warm clouds inherently require some amount of time to grow to a given depth. If more time is necessary for deeper warm clouds to achieve their greater altitudes, the amount of time available for warm rain processes to act within these clouds would also be increased—a factor that is critical to the production of warm rainfall (e.g., Reiche and Lasher-Trapp 2010; Burnet and Brenguier 2010). The composite relationships between cloud depth and rainfall occurrence derived within this section are inherently representative of clouds in various stages of development, maturity, and decay. As they were produced from averaging many snapshot scenes, it is not known, for instance, what percentage of 1-km-deep clouds ascended to greater depths or produced rainfall at later times. The relationships between cloud life cycle, cloud macrophysical characteristics, and rainfall are explored in further detail within section 4.

c. Relationship with cloud layer attenuation

Thus far, it has been shown that the likelihood of warm rainfall from *CloudSat*-observed and RAMS-simulated liquid-phase clouds increased with both increasing PIA (Fig. 4) and increasing cloud depth (Fig. 5). However, these two cloud macrophysical characteristics are, in the mean, directly related to one another (Fig. 6). The aim of this section is to investigate the relative role of each characteristic by analyzing the joint probability that warm clouds with given pairs of PIA and depth

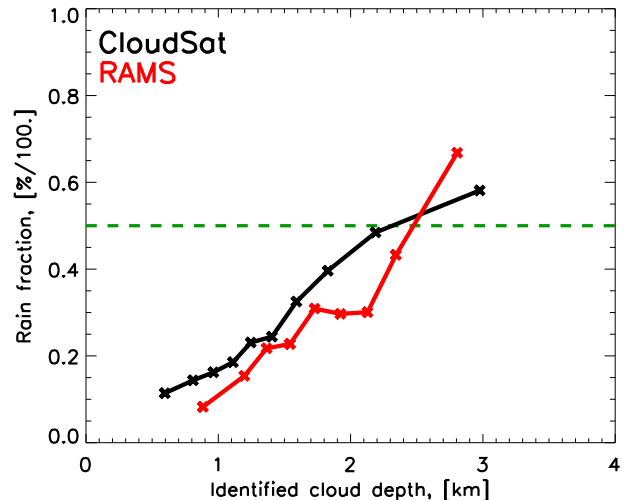


FIG. 5. Rain fraction as a function of deciles of cloud depth for *CloudSat* (black) and RAMS (red) warm clouds. Nodes represent the median cloud depth in each cloud depth decile bin.

attributes produced rainfall. In doing so, insight was gained on how the concentration of liquid water within these observed and simulated warm clouds influenced their propensity to precipitate.

The methodology developed to investigate these joint probabilities of rainfall relied upon sequential decile partitions of the warm cloud datasets with respect to PIA and cloud depth. First, decile values of PIA were identified for the *CloudSat* and RAMS warm cloud distributions, and these decile values were used to define PIA bin boundaries. Within each identified PIA decile bin, decile values of cloud depth were calculated and used to define corresponding cloud depth bin boundaries. With these two decile-partitioning steps complete, each PIA–cloud depth decile bin pair within the *CloudSat* and RAMS datasets contained approximately 181 000 and 708 000 warm cloud scenes, respectively.

The execution of these two distinct partitioning steps stratified the observed and simulated warm cloud distributions in physically meaningful ways. Mean values of RAMS in-cloud averaged total water content (TWC; the sum of cloud, drizzle and rainwater contents) as a function of deciles of cloud depth within each PIA decile bin (colored curves) are shown in Fig. 7. For approximately constant PIA (along any given colored curve), the mean in-cloud averaged TWC decreases with increasing cloud depth, as expected. Crude estimates of *CloudSat* cloud-mean TWC derived for an analysis discussed within section 5 were qualitatively consistent with the RAMS-derived trends in Fig. 7.

The fractional occurrence of warm rainfall as a function of cloud depth, stratified by PIA, is shown in Fig. 8. Beginning with the RAMS trends in Fig. 8b, for any

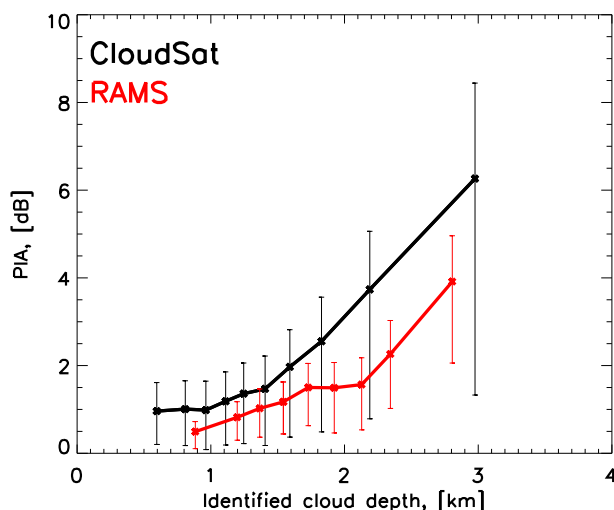


FIG. 6. PIA as a function of deciles of cloud depth for *CloudSat* (black) and RAMS (red) warm clouds. Thick curves represent the mean trend. Nodes along these curves represent the median cloud depth within each cloud depth decile bin. Lower and upper bars represent the 25th and 75th PIA percentiles, respectively, within each cloud depth decile bin.

given cloud depth, simulated warm rainfall was increasingly more likely with increasing PIA, as the amount of liquid water available for warm rain processes increased in this direction (Figs. 6 and 7). Along any given approximately constant PIA curve, RAMS warm rainfall generally became less likely—or, in the case of the lowest PIA bins, remained equally unlikely—as cloud depth increased. Intuitively, warm rainfall was less probable when the same amount of water was spread over a deeper simulated cloud layer, as this scenario resulted in lower mean in-cloud averaged TWC. These trends collectively underscore the importance of liquid water availability for the production of warm rainfall within RAMS.

Despite comparable PIA and cloud depth decile bins, the fractional occurrences of warm rainfall derived from the *CloudSat* dataset (Fig. 8a) are, at first glance, drastically different from those characterizing warm clouds simulated with RAMS. While observed warm rainfall from clouds of the same depth was also increasingly more likely with increasing PIA, the magnitude of this increase was less pronounced than it was in the RAMS trends (Fig. 8b). As was shown in section 3a, the likelihood of rain from RAMS-simulated warm clouds increased more sharply as a function of increasing PIA than observations indicated (Fig. 4). These results suggest that simulated warm rain processes too efficiently converted cloud water to rain (Suzuki et al. 2011).

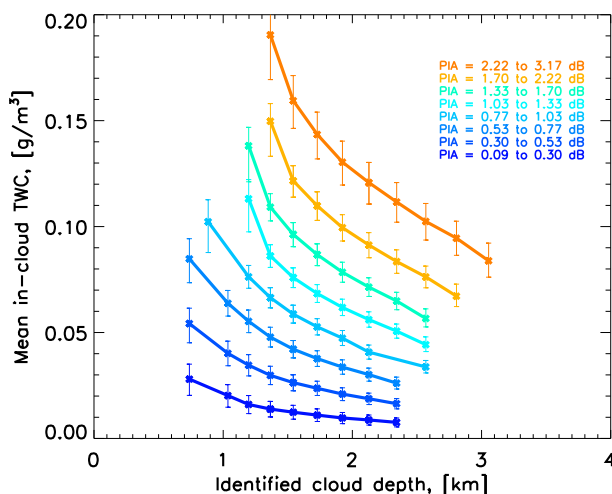


FIG. 7. Mean in-cloud averaged TWC as a function of deciles of cloud depth, stratified by deciles of PIA (colored curves) for RAMS warm clouds. Nodes along each PIA curve represent the median cloud depth within each cloud depth decile bin. Lower and upper bars represent the 25th and 75th TWC percentiles, respectively, within each joint PIA–cloud depth bin.

At similar values of observed and simulated PIA, the variation of *CloudSat* warm rainfall likelihood with respect to cloud depth was markedly different than that from RAMS. Along most of the lower *CloudSat* PIA decile bin curves in Fig. 8a, the fractional occurrence of rainfall actually increased with increasing warm cloud depth, in contrast to the RAMS-derived relationships in Fig. 8b. This would imply that deeper observed warm clouds with the same PIA as their shallower counterparts were actually more likely to rain, despite likely having lower average concentrations of liquid water mass within their volumes (Fig. 7). While the likelihood of RAMS-simulated warm rainfall is strongly governed by the availability of water within a cloud, these trends suggest that such a relationship is not as clearly defined for clouds observed within nature. In contrast to the low PIA trends, *CloudSat*-observed rainfall likelihood as a function of cloud depth within the highest PIA decile bin was more similar to that from RAMS; rainfall generally became less likely along this high PIA curve as cloud depth increased past ~ 1.25 km.

To ensure that these *CloudSat*–RAMS rainfall occurrence trend differences were not simply related to the nature of the warm cloud observations themselves, the *CloudSat* distribution was further constrained through a series of experiments designed to facilitate more direct comparisons with the RAMS warm cloud distribution (Table 2). While the RAMS RCE simulation was initialized with a sounding characteristic of the mean tropical atmosphere and utilized a fixed sea surface temperature (SST) of 300 K (section 2b), the surprising *CloudSat* rainfall occurrence trends in Fig. 8a held

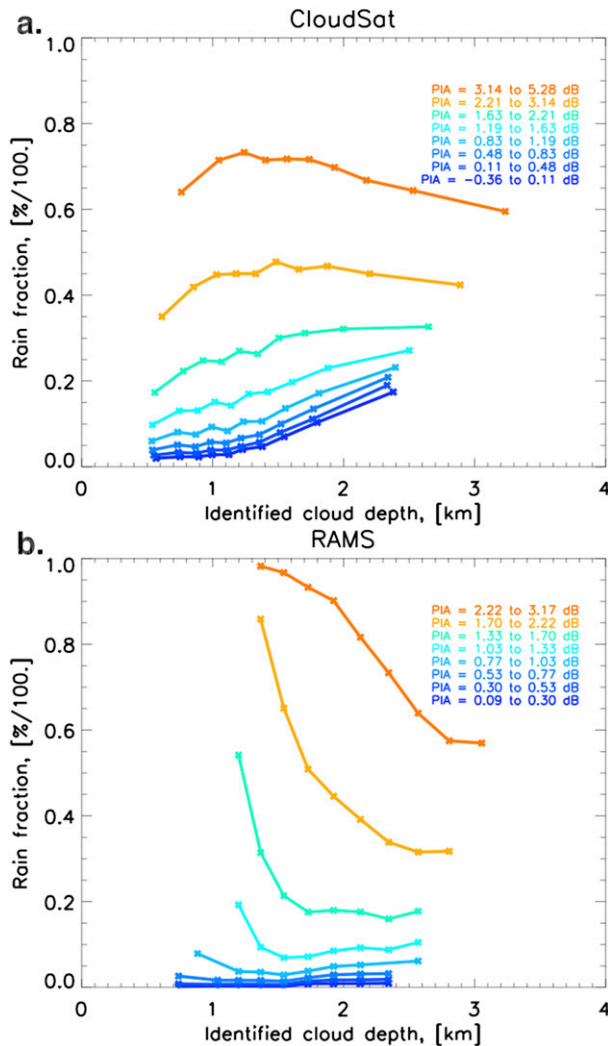


FIG. 8. Rain fraction as a function of deciles of cloud depth, stratified by deciles of PIA (colored curves) for warm clouds (a) observed by *CloudSat* and (b) simulated with RAMS. Nodes along each PIA curve represent the median cloud depth within each cloud depth decile bin.

when the warm cloud distribution was constrained to observations made either within the tropics (from 20°N to 20°S) or on a corresponding SST interval (300 ± 0.25 K). *CloudSat* crosses the equator at ~ 1330 and ~ 0130 local time on the ascending and descending segments of its sun-synchronous orbit, respectively. Segregation of the *CloudSat* warm cloud observations into ascending (daytime) and descending (nighttime) orbit groups to assess the magnitude of day or night dependencies within the observational dataset yielded rainfall occurrence trends that were nearly identical to those in Fig. 8a.

An additional lower-tropospheric static stability (LTSS) stratification experiment was performed (Table

TABLE 2. Additional *CloudSat* warm cloud subsetting experiments and associated resulting distribution metrics.

Stratification	Total warm cloud counts	Rain fraction
None (reference)	1.81×10^7	28.7%
SST = 300 ± 0.25 K	8.04×10^5	37.4%
Tropics (20°N–20°S)	8.10×10^6	32.8%
Ascending overpasses	6.97×10^6	29.5%
Descending overpasses	1.12×10^7	28.2%
High LTSS ($>19.5^\circ\text{C}$)	3.73×10^6	19.1%
Low LTSS ($<14.4^\circ\text{C}$)	3.59×10^6	33.9%

2) to ensure that the increase in observed rain fraction with cloud depth within the lowest PIA decile bins was not an artifact of averaging warm cloud properties across different atmospheric thermodynamic regimes. For each observed warm cloud, LTSS was calculated from ancillary *CloudSat* ECMWF-AUX data as the potential temperature difference between 700 hPa and the surface (e.g., Lebock et al. 2008). As is shown in Fig. 9, clouds observed within environments with the 20% highest LTSS (LTSS $\geq 19.5^\circ\text{C}$) were generally shallower, had lower PIA, and rained less often than those observed within the 20% lowest LTSS environments (LTSS $\leq 14.4^\circ\text{C}$), as expected. However, within both LTSS groups, rain fraction increased with increasing cloud depth within the lowest PIA decile bins (Fig. 9) in a manner that was still inconsistent with the trends from RAMS (Fig. 8b).

The *CloudSat*-derived results presented within this section were largely counterintuitive. The remainder of this paper is devoted to examining what insight on these cloud macrophysical–rainfall occurrence relationships may be gained through a more direct examination of cloud life cycle.

4. Toward better understanding cloud life cycle

Cumulus cloud life cycle is often conceptualized as consisting of three stages: growth, maturity, and dissipation (e.g., Malkus 1952; Byers and Hall 1955; Heus et al. 2009; Cotton et al. 2010; Witte et al. 2014; Katzwinkel et al. 2014; Borque et al. 2014). Within this construct, incipient clouds increase in depth through their growth stage, cease growth and precipitate any rain hydrometeors they have managed to develop during their mature phase, and break apart as a result of factors such as water mass rainout and/or entrainment in their dissipation stage. Thus, while the production of rainfall from warm clouds in this simple view is related to cloud depth—and, by association, TWP or PIA (Fig. 6)—it is ultimately dependent upon another critical, and perhaps all encompassing, factor: time. As all of the *CloudSat* and RAMS composite cloud macrophysical–rainfall

occurrence relationships presented within previous sections were derived from many individual snapshot captures of observed and simulated warm clouds, they are inherently representative of the collective amount of time clouds spent within these various life stages. The aim of this section is to explore the ways in which differences in the evolution of modeled and observed warm clouds through these life stages account for the differences in simulated and observed rainfall occurrence statistics discussed in section 3c.

In their terminal–transient analysis framework, Luo et al. (2009) calculated cloud-top temperature differences for *CloudSat*-identified cumulus congestus clouds by making use of collocated A-Train observations and ECMWF reanalysis data. Cloud-top height measurements from *CloudSat* were used in conjunction with ECMWF-AUX environmental temperature profiles to determine the environmental temperature T_{env} at cloud-top height. Collocated MODIS brightness temperatures were then used to calculate cloud-top temperature (CTT) for each *CloudSat*-identified deep convective cloud, under the assumption that limited cloud-top emissivity caused radar-derived cloud tops to be ~ 1 km higher or, following moist adiabatic lapse rate arguments, ~ 6 K cooler than these brightness temperatures would suggest.

The methodology used to assess warm cloud maturity within the present study closely resembles that of Luo et al. (2009). However, in comparison to the cloud-top temperature differences characterizing the more vigorously convecting cumulus congestus clouds examined within the earlier study, the magnitudes of the analogous temperature differences for the warm clouds analyzed here are likely significantly smaller, potentially bordering upon the magnitude of the uncertainties in the observationally based methodology itself. Thus, instead of directly applying the same procedure outlined by Luo et al. (2009) to warm clouds observed by *CloudSat*, a similar cloud-top temperature difference analysis was carried out only for RAMS-simulated warm clouds. For each identified RAMS warm cloud, CTT was simply defined as the temperature at the analyzed cloud-top height. The corresponding T_{env} for each of these clouds was then calculated by averaging noncloudy model temperatures for grid boxes at the same cloud-top altitude within a $15 \text{ km} \times 15 \text{ km}$ box surrounding the cloud of interest. Estimates of T_{env} were calculated from an average of ~ 56 neighboring noncloudy model grid points within these search boxes.

Through this methodology, 21.5% of the entire RAMS warm cloud distribution was found to be characterized by $\text{CTT} > T_{env}$ (positive buoyancy). To compare positively and negatively buoyant RAMS-simulated warm clouds, two subsets were drawn from

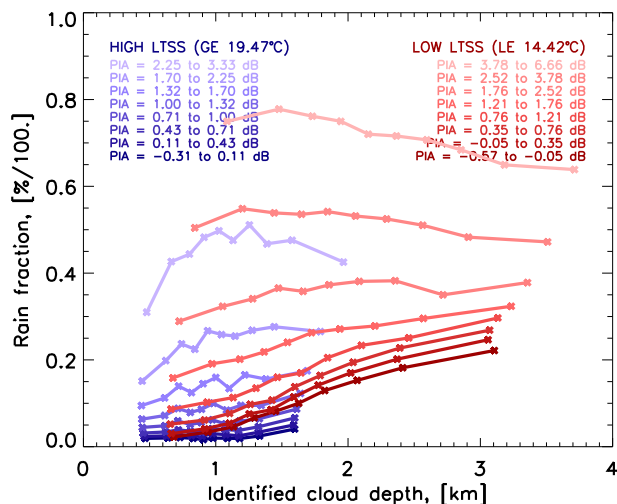


FIG. 9. As in Fig. 8a, but for *CloudSat*-observed warm clouds associated with the 20% highest (blue) and 20% lowest (red) LTSS.

the high- and low-end tails of this cloud-top buoyancy distribution. Because the overall distribution was heavily weighted toward negatively buoyant clouds, the 2.5% most buoyant RAMS-simulated warm clouds, those with CTTs 0.47 K or more warmer than their surrounding environments, were chosen to represent the positively buoyant subset (hereafter, POSbuoyant). Correspondingly, the 2.5% least buoyant warm clouds, those with CTTs 1.69 K or more cooler than their surrounding environments, were chosen to represent the negatively buoyant subset (hereafter, NEGbuoyant). All results derived from these subsets were found to be qualitatively similar to those derived from the 10% most positively and negatively buoyant simulated clouds within the full cloud-top buoyancy distribution.

The likelihood of rainfall from warm clouds simulated with RAMS was found to be related to cloud-top buoyancy (Fig. 10a). Rainfall was most probable from the RAMS clouds that were most negatively buoyant at cloud top. Physically, this result is in line with the conceptual view of cloud life cycle outlined at the beginning of this section and implies that rain is more likely to fall from mature or decaying clouds. The difference between the NEGbuoyant and POSbuoyant cloud-top normalized mean reflectivity profiles in Fig. 10b provides further evidence for this assertion. Higher reflectivity values within the vast majority of the NEGbuoyant cloud column indicate that these clouds were characterized by larger liquid hydrometeors than were found within the POSbuoyant subset.

The overall RAMS warm rainfall occurrence trends in Fig. 8b were recalculated for the NEGbuoyant and POSbuoyant subsets. The RAMS NEGbuoyant rain fraction relationships in Fig. 11a largely mirror the

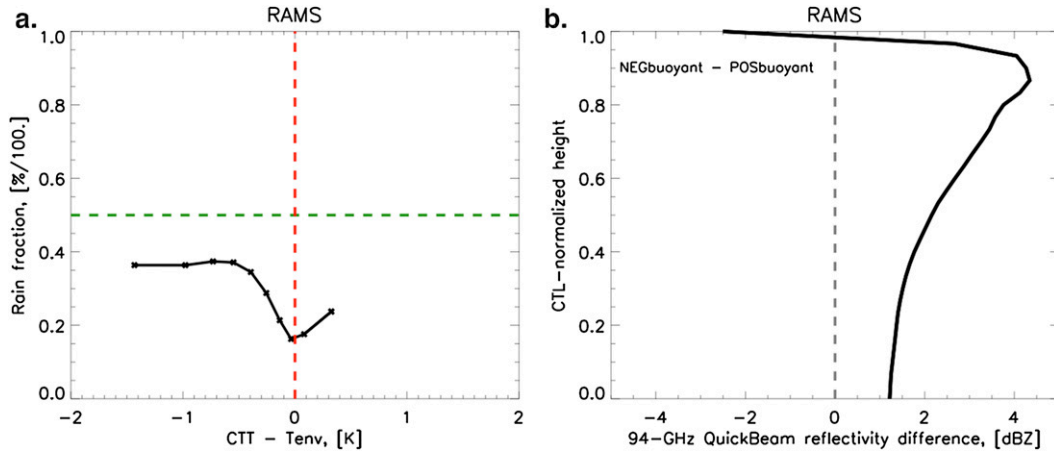


FIG. 10. (a) Rain fraction as a function of deciles of the temperature difference between CTT and T_{env} for RAMS warm clouds. (b) Profile difference of the mean QuickBeam RAMS reflectivity profiles for the NEGbuoyant [(CTT - T_{env}) \leq -1.69 K] minus POSbuoyant [(CTT - T_{env}) \geq 0.47 K] subsets. Before averaging, height profiles were normalized by individual identified cloud-top heights (CTL) to account for clouds of differing depths.

general RAMS trends in Fig. 8b. As the majority of the clouds within the entire RAMS cloud distribution were negatively buoyant at cloud top, it was no surprise that rainfall occurrence trends from these negatively buoyant clouds so closely mirrored those from the general warm cloud case.

Rainfall occurrence trends characterizing the POSbuoyant RAMS warm cloud subset in Fig. 11b displayed features more characteristic of the *CloudSat*-derived relationships in Fig. 8a. Similar to the rain fraction trends derived from the overall RAMS (Fig. 8b) and *CloudSat* (Fig. 8a) cloud distributions, rain fraction within the highest PIA decile bins still decreased with increasing cloud depth. However, within the lowest PIA decile bins, rain was more likely to fall from deeper clouds, similar to the overall *CloudSat* rainfall

occurrence trends (Fig. 8a). If clouds are positively buoyant and, thus, growing, then perhaps deeper growing clouds with similar, or even slightly higher PIA values than their shallower counterparts have simply had more time to produce rainfall. When clouds contain large amounts of liquid water (high PIA), the greater availability of liquid water likely promotes a vigorous, more rapid conversion of cloud water to rainwater.

The cloud-top normalized reflectivity profile differences in Fig. 12 provide further evidence for cloud maturity being the cause for the unexpected increase in rain fraction as a function of cloud depth within the lowest PIA decile bins for the *CloudSat* and POSbuoyant RAMS distributions (Figs. 8a and 11b, respectively). For observed and POSbuoyant simulated clouds with PIA values less than 1 dB, a cloud depth value of 1.5 km was

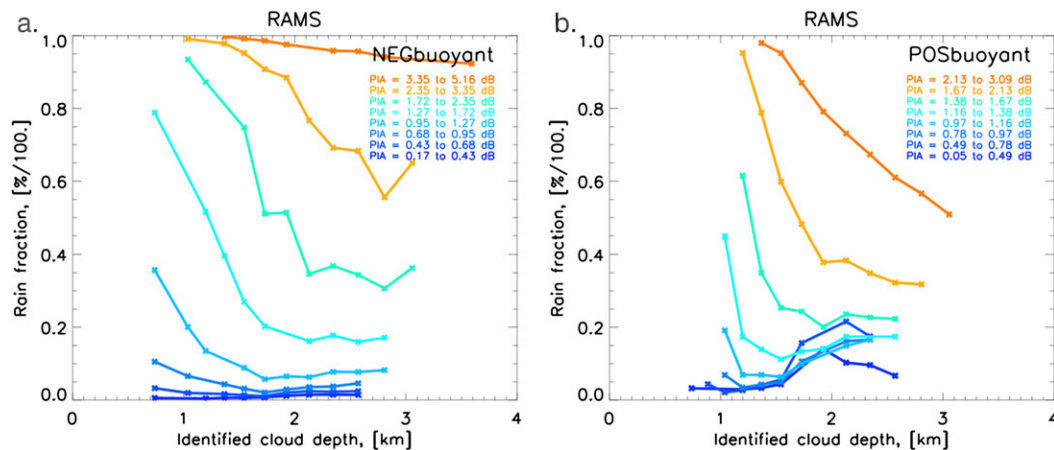


FIG. 11. As in Fig. 8b, but for the (a) NEGbuoyant and (b) POSbuoyant RAMS-simulated warm clouds.

used to separate the remaining distributions into shallow and deep groups. The deep groups within each subset were more likely to rain than their shallow counterparts, despite lower cloud-mean TWC. Figure 12 shows the mean cloud-top normalized reflectivity profile for the deep subset minus the corresponding mean profile for the shallow subset within the overall *CloudSat* and POSbuoyant RAMS distributions. Deeper clouds in the observed and modeled distributions were generally characterized by higher reflectivities below cloud top than their shallower counterparts—in line with the RAMS NEGbuoyant–POSbuoyant reflectivity profile differences in Fig. 10b. These results suggest that as these clouds developed in time, hydrometeors within deeper, more mature clouds grew larger and were located lower than those found within their shallower, incipient stage counterparts.

Collectively, these results implied that warm clouds observed by *CloudSat* spent more time in their growth stage than did those simulated with RAMS. That the majority of RAMS warm clouds were found to be negatively buoyant at cloud top suggested that simulated clouds matured, and produced rainfall, more quickly than did those observed in nature through the lens of *CloudSat*.

5. Discussion and conclusions

In this study, modeled and observed warm, maritime rainfall occurrence and its composite statistical relationships with cloud macrophysical properties were analyzed. It was shown that approximately one-quarter of the *CloudSat*-observed and RAMS-simulated warm, single-layered clouds produced rainfall and that this rainfall was increasingly more likely when these clouds contained greater amounts of column-integrated water mass (as represented by PIA). This supports a growing body of evidence that the probability of warm rainfall steadily increases as a function of column-integrated water mass (Lebsock et al. 2008; L'Ecuyer et al. 2009; Kubar et al. 2009; Suzuki et al. 2011). However, RAMS-simulated warm clouds rained more frequently at lower PIA values than observations indicated, suggesting that the parameterized cloud-to-rain conversion processes within RAMS produce rainfall more readily than was observed in nature (Suzuki et al. 2011). While modeled and observed warm rain was more likely to fall from deeper clouds, these deeper clouds were associated with higher mean PIA values, suggesting that the increased availability of liquid water was one factor that preferentially supported more active warm rain processes within clouds of the greatest vertical extent.

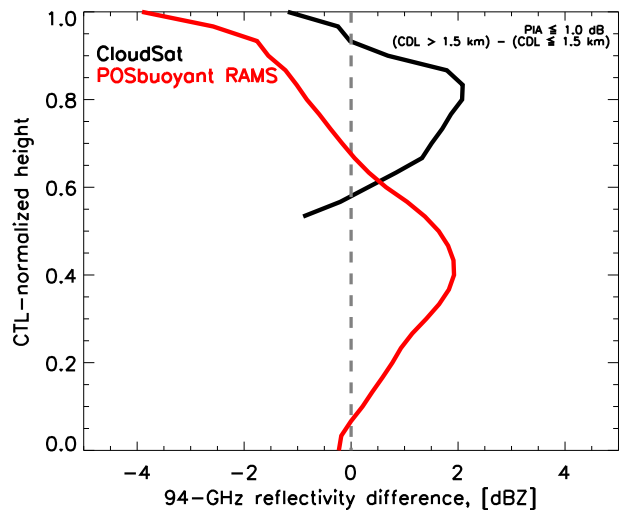


FIG. 12. For *CloudSat* (black) and POSbuoyant RAMS (red) warm clouds with $\text{PIA} \leq 1.0$ dB, the difference of the mean reflectivity profiles from clouds with depths >1.5 km minus clouds with depths ≤ 1.5 km. Before averaging, height profiles were normalized by individual identified cloud-top heights to account for clouds of differing depths. While 2B-GEOPROF-identified surface clutter was screened from the *CloudSat* profiles and did not contribute to these means, normalized height layers with more than 5% of profiles flagged as surface clutter were conservatively excluded from the *CloudSat* profile difference curve.

The calculation of rain fraction as a joint function of PIA and cloud depth revealed significant differences between the model and observations that effectively highlighted differing rainfall production sensitivities to the mean density of liquid water within the cloudy column. RAMS-simulated warm rain was most probable when a large amount of liquid water was confined to a shallow cloud layer, as this combination resulted in the highest cloud-mean TWC and, thus, likely supported vigorous warm rain coalescence processes. While water availability was certainly one factor that determined an observed warm cloud's propensity to produce rainfall, another intervening factor related to cloud depth seemed nearly as critical when PIA was low.

The same *CloudSat* and RAMS warm rainfall occurrence statistics in Fig. 8 can alternatively be plotted as a simultaneous function of cloud-mean TWC and cloud depth (Fig. 13). For the *CloudSat* trends in Fig. 13a, mean in-cloud TWC was estimated by first obtaining an estimate of *CloudSat* TWP from PIA using the linear form $\text{TWP} \approx c(\text{PIA})$, where $c = 107.5 \text{ g m}^{-2} \text{ dB}^{-1}$ and was derived from the RAMS relationships in Fig. 3. These TWP estimates were then divided by the depth of each observed cloud to obtain crude estimates of in-cloud-mean *CloudSat* TWC. The rainfall occurrence trends in Fig. 13 directly indicate that warm rainfall within RAMS is more strongly governed by

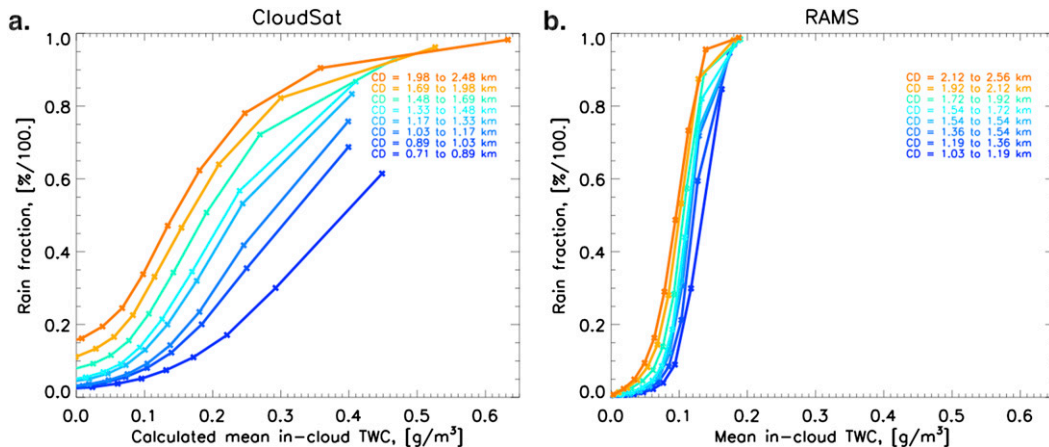


FIG. 13. Rain fraction as a function of deciles of in-cloud-mean TWC, stratified by deciles of cloud depth (colored curves) for warm clouds (a) observed by *CloudSat* and (b) simulated with RAMS. Nodes along each cloud depth curve represent the median in-cloud-mean TWC values within each in-cloud-mean TWC decile bin. While RAMS TWC values were obtained directly from model output, *CloudSat* TWC estimates were derived from PIA and cloud depth. See text for details.

the concentration of liquid water within the cloud than observations suggest.

Further stratification of the RAMS warm cloud distribution by cloud-top buoyancy provided insight into how these composite warm rainfall occurrence statistics were influenced by cloud life cycle. Rainfall likelihoods for positively buoyant simulated clouds exhibited properties more similar to those characterizing the overall observed cloud distribution than did those derived from the negatively buoyant simulated subset. This prompted the suggestion that the *CloudSat* warm cloud distribution was likely characterized by greater proportions of positively buoyant, developing clouds.

Based on these results, a conceptual representation of the temporal evolution of observed and simulated warm clouds was developed (Fig. 14). In short, it is hypothesized that warm clouds observed within nature mature more gradually in time than do those simulated with RAMS. While increasing liquid water contents trigger the rapid development of rainfall within RAMS clouds, the same liquid water contents do not so readily support actual rain production (e.g., time t_2 in Fig. 14). If these cloud distributions were sampled randomly, it is expected that *CloudSat* would observe greater proportions of developing (positively buoyant) cloud scenes than are represented within the comparable RAMS cloud distribution.

Throughout this study, it has been assumed that the three-dimensional resolutions of the *CloudSat* and RAMS datasets were similar enough to one another to permit direction comparisons and sufficient enough to resolve warm clouds. While *CloudSat* observes the real atmosphere within its $1.7\text{ km} \times 1.4\text{ km}$ horizontal field of view

and 240-m vertical range gate spacing, the atmosphere is resolved at a 1-km horizontal resolution and a stretched vertical grid within the RAMS RCE simulation. Although it is argued that the similarity of these scales is valuable when comparing a large statistical sample from the two datasets over representative spatial domains, rainfall from shallow clouds is known to vary on horizontal scales much finer than the model and observational resolutions analyzed herein (e.g., Rauber et al. 2007; Zuidema et al. 2012). While it is difficult to quantify the bias introduced by these resolutions and their differences, relevant processes that are difficult to faithfully observe remotely and resolve in a model at these scales likely include entrainment, turbulence, sedimentation, and updraft velocity. Moreover, observational sensitivity and subfield of view inhomogeneity in the cloud field [see MODIS-based *CloudSat* scene homogeneity methods in Kubar et al. (2009) and Lebsock et al. (2011)] could conceivably skew the observational results accordingly.

In an initial attempt to assess the magnitude of the bias introduced by horizontal resolution differences between *CloudSat* and RAMS, an experiment was performed wherein the native 1-km horizontal resolution RAMS output was averaged over a *CloudSat*-like field of view of $2\text{ km} \times 1\text{ km}$. If either RAMS cloud scene within this effective field of view was identified as raining, the resulting averaged scene was flagged as raining. While this averaging resulted in a 6.3% increase in the overall RAMS rain fraction to 33.6%, the RAMS rainfall occurrence results in Figs. 4, 5, and 8b remained qualitatively consistent for this averaged RAMS distribution. Therefore, we conclude that if progress is to be

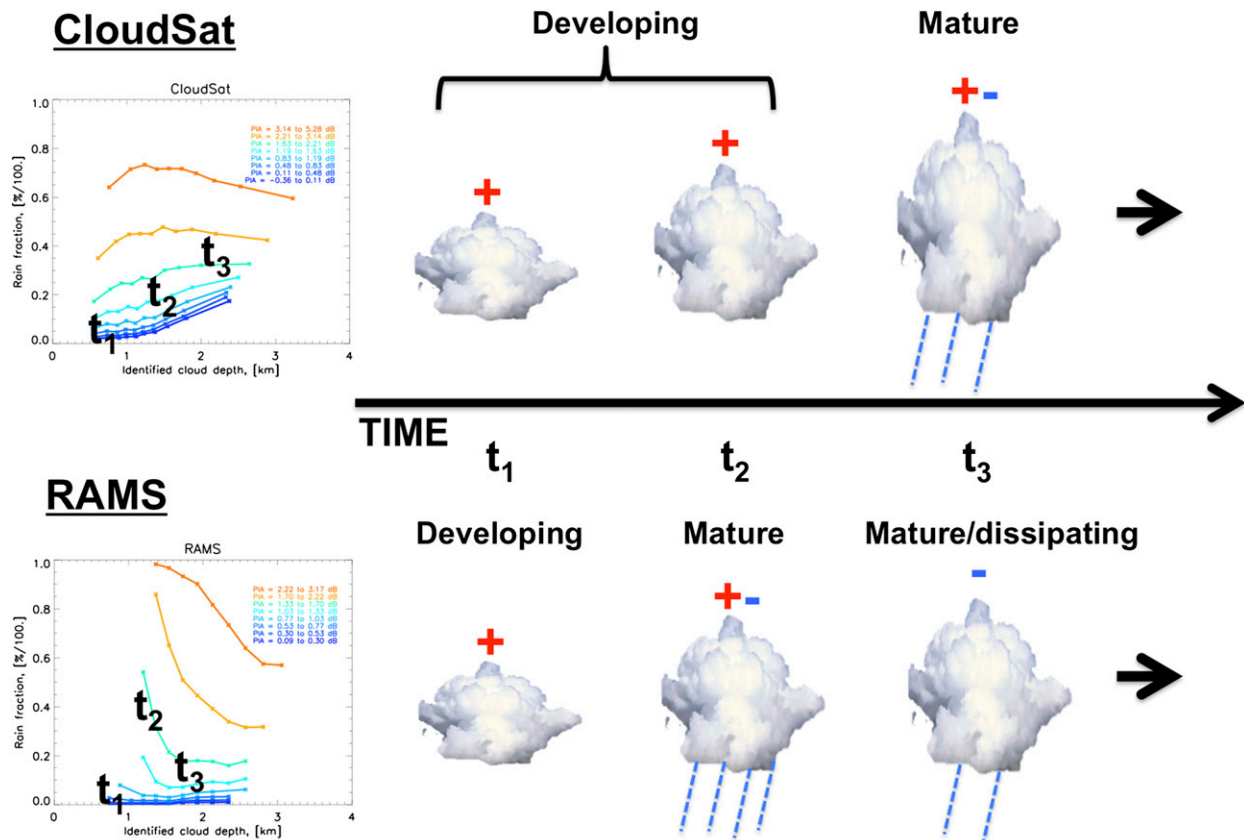


FIG. 14. Schematic representation of the proposed composite temporal evolution of *CloudSat*-observed and RAMS-simulated warm clouds. Positive, neutral, and negative cloud-top buoyancy are denoted by plus (+), plus and minus (+ -), and minus (-) symbols, respectively.

made in evaluating model performance in simulating shallow clouds and their rainfall on near-global scales, it is advantageous if the resolution of the simulation is readily verifiable against observations obtained over climatically relevant spatial and temporal scales, as is done here.

While the *CloudSat*-derived rainfall occurrence trends were found to be insensitive to whether the observations were taken during ascending (~ 1330 local time equatorial crossing) or descending (~ 0130 local time equatorial crossing) orbit portions, *CloudSat* cannot be used to analyze the full diurnal cycle of warm clouds and their rainfall. The consistency of the results corresponding to these two times, however, suggests that it is unlikely that the composite character of life cycle for these warm, maritime clouds changes appreciably between the daytime and the nighttime. Future observational research on cloud life cycle would nonetheless benefit from observations of the full diurnal cycle to rule out a potential diurnal bias.

Although it is expected that the cloud-top temperature difference methodology used within this study should

give a crude indication of the distribution of cloud maturity, the cloud life cycle ideas developed herein would greatly benefit from more direct measurements of cloud evolution. Within RAMS, a cloud-tracking algorithm (e.g., [Dawe and Austin 2012](#); [Witte et al. 2014](#)) could be developed to trace the full life cycle of simulated warm clouds and identify temporal rainfall onset. Methodologies designed to track cloud features observed by satellites in time are inherently hindered by the nature of the observations themselves. While it is conceivable that *CloudSat* observations of warm clouds could be combined with ancillary satellite data to track cloud features in time, the limited spatial and temporal resolutions of these satellite datasets may inhibit such efforts. Additional observational insight into warm cloud evolution may be better achieved through the analysis of surface-based measurements (e.g., [Borque et al. 2014](#)).

The two-moment microphysical scheme employed by RAMS within the present study is based upon bin microphysics—the current benchmark for all microphysical schemes. Moreover, [Suzuki et al. \(2011\)](#) showed that

this RAMS scheme markedly outperformed a simpler, single-moment Kessler-type microphysical scheme used within NICAM in the realism of its depiction cloud-to-rainwater conversion. Thus, while this study concludes that RAMS-parameterized warm rain processes produced rainfall more efficiently and more quickly than was suggested by *CloudSat* observations, such behavior is likely to be more pronounced in models with less sophisticated microphysical schemes.

Acknowledgments. The authors thank three anonymous reviewers for many insightful comments that improved the quality of this manuscript. This work was supported by the National Aeronautics and Space Administration under Grant NNX11AF06G and by the National Science Foundation under Grant AGS-1005316. M. Igel was supported by NASA Headquarters under the NASA Earth and Space Science Fellowship Program Grant NNX 13AN66H. M. Igel and S. van den Heever were also supported by NASA Grant 5-319160.

REFERENCES

- Albrecht, B., C. W. Fairall, D. W. Thomson, A. B. White, J. B. Snider, and W. H. Schubert, 1990: Surface-based remote sensing of the observed and the adiabatic liquid water content of stratocumulus clouds. *Geophys. Res. Lett.*, **17**, 89–92, doi:10.1029/GL017i001p00089.
- Berg, W., T. L'Ecuyer, and J. M. Haynes, 2010: The distribution of rainfall over oceans from spaceborne radars. *J. Appl. Meteor. Climatol.*, **49**, 535–543, doi:10.1175/2009JAMC2330.1.
- Bony, S., and J. Dufresne, 2005: Marine boundary layer clouds at the heart of tropical cloud feedback uncertainties in climate models. *Geophys. Res. Lett.*, **32**, L20806, doi:10.1029/2005GL023851.
- Borque, P., P. Kollias, and S. Giangrande, 2014: First observations of tracking clouds using scanning ARM cloud radars. *J. Appl. Meteor. Climatol.*, **53**, 2732–2746, doi:10.1175/JAMC-D-13-0182.1.
- Burnet, F., and J.-L. Brenguier, 2010: The onset of precipitation in warm cumulus clouds: An observational case-study. *Quart. J. Roy. Meteor. Soc.*, **136**, 374–381, doi:10.1002/qj.552.
- Byers, H., and R. Hall, 1955: A census of cumulus cloud height versus precipitation in the vicinity of Puerto Rico during the winter and spring of 1953–1954. *J. Meteor.*, **12**, 176–178, doi:10.1175/1520-0469(1955)012<0176:ACOCCH>2.0.CO;2.
- Chen, R., Z. Li, R. J. Kuligowski, R. Ferraro, and F. Weng, 2011: A study of warm rain detection using A-Train satellite data. *Geophys. Res. Lett.*, **38**, L04804, doi:10.1029/2010GL046217.
- Christensen, M. W., G. L. Stephens, and M. D. Lebsock, 2013: Exposing biases in retrieved low cloud properties from *CloudSat*: A guide for evaluating observations and climate data. *J. Geophys. Res. Atmos.*, **118**, 12 120–12 131, doi:10.1002/jgra.50317.
- Cotton, W. R., and Coauthors, 2003: RAMS 2001: Current status and future directions. *Meteor. Atmos. Phys.*, **82**, 5–29, doi:10.1007/s00703-001-0584-9.
- , G. H. Bryan, and S. C. van den Heever, 2010: *Storm and Cloud Dynamics*. 2nd ed. Academic Press, 820 pp.
- Dawe, J. T., and P. H. Austin, 2012: Statistical analysis of an LES shallow cumulus cloud ensemble using a cloud tracking algorithm. *Atmos. Chem. Phys.*, **12**, 1101–1119, doi:10.5194/acp-12-1101-2012.
- Feingold, G., R. L. Walko, B. Stevens, and W. R. Cotton, 1998: Simulations of marine stratocumulus using a new microphysical parameterization scheme. *Atmos. Res.*, **47–48**, 505–528, doi:10.1016/S0169-8095(98)00058-1.
- Hartmann, D. L., M. E. Ockert-Bell, and M. L. Michelsen, 1992: The effect of cloud type on Earth's energy balance: Global analysis. *J. Climate*, **5**, 1281–1304, doi:10.1175/1520-0442(1992)005<1281:TEOCTO>2.0.CO;2.
- Haynes, J. M., and G. L. Stephens, 2007: Tropical oceanic cloudiness and the incidence of precipitation: Early results from *CloudSat*. *Geophys. Res. Lett.*, **34**, L09811, doi:10.1029/2007GL029335.
- , R. T. Marchand, Z. Luo, A. Bodas-Salcedo, and G. L. Stephens, 2007: A multipurpose radar simulation package: QuickBeam. *Bull. Amer. Meteor. Soc.*, **88**, 1723–1727, doi:10.1175/BAMS-88-11-1723.
- , T. S. L'Ecuyer, G. L. Stephens, S. D. Miller, C. Mitrescu, N. B. Wood, and S. Tanelli, 2009: Rainfall retrieval over the ocean with spaceborne W-band radar. *J. Geophys. Res.*, **114**, D00A22, doi:10.1029/2008JD009973.
- Heus, T., H. J. J. Jonker, H. E. A. van den Akker, E. J. Griffith, M. Koutek, and F. H. Post, 2009: A statistical approach to the life cycle analysis of cumulus clouds selected in a virtual reality environment. *J. Geophys. Res.*, **114**, D06208, doi:10.1029/2008JD010917.
- Igel, A. L., M. R. Igel, and S. C. van den Heever, 2015: Make it a double? Sobering results from simulations using single-moment microphysics schemes. *J. Atmos. Sci.*, **72**, 910–925, doi:10.1175/JAS-D-14-0107.1.
- Im, E., S. L. Durden, and C. Wu, 2005: Cloud profiling radar for the *CloudSat* mission. *IEEE Aerosp. Electron. Syst.*, **20**, 15–18, doi:10.1109/MAES.2005.1581095.
- Katzwinkel, J., H. Siebert, T. Heus, and R. A. Shaw, 2014: Measurements of turbulent mixing and subsiding shells in trade wind cumuli. *J. Atmos. Sci.*, **71**, 2810–2822, doi:10.1175/JAS-D-13-0222.1.
- Kessler, E., 1969: *On the Distribution and Continuity of Water Substance in Atmosphere Circulation*. *Meteor. Monogr.*, No. 32, Amer. Meteor. Soc., 84 pp.
- Kubar, T. L., D. L. Hartmann, and R. Wood, 2009: Understanding the importance of microphysics and macrophysics for warm rain in marine low clouds. Part I: Satellite observations. *J. Atmos. Sci.*, **66**, 2953–2972, doi:10.1175/2009JAS3071.1.
- Lau, K., and H. Wu, 2003: Warm rain processes over tropical oceans and climate implications. *Geophys. Res. Lett.*, **30**, 2290, doi:10.1029/2003GL018567.
- Lebsock, M. D., and T. S. L'Ecuyer, 2011: The retrieval of warm rain from *CloudSat*. *J. Geophys. Res.*, **116**, D20209, doi:10.1029/2011JD016076.
- , G. L. Stephens, and C. Kummerow, 2008: Multisensor satellite observations of aerosol effects on warm clouds. *J. Geophys. Res.*, **113**, D15205, doi:10.1029/2008JD009876.
- , T. S. L'Ecuyer, and G. L. Stephens, 2011: Detecting the ratio of rain and cloud water in low-latitude shallow marine clouds. *J. Appl. Meteor. Climatol.*, **50**, 419–432, doi:10.1175/2010JAMC2494.1.

- L'Ecuyer, T. S., W. Berg, J. Haynes, M. Lebsock, and T. Takemura, 2009: Global observations of aerosol impacts on precipitation occurrence in warm maritime clouds. *J. Geophys. Res.*, **114**, D09211, doi:10.1029/2008JD011273.
- Leon, D. C., Z. Wang, and D. Liu, 2008: Climatology of drizzle in marine boundary layer clouds based on 1 year of data from *CloudSat* and *Cloud-Aerosol Lidar and Infrared Pathfinder Satellite Observations (CALIPSO)*. *J. Geophys. Res.*, **113**, D00A14, doi:10.1029/2008JD009835.
- Liu, C., and E. J. Zipser, 2009: "Warm rain" in the tropics: Seasonal and regional distributions based on 9 yr of TRMM data. *J. Climate*, **22**, 767–779, doi:10.1175/2008JCLI2641.1.
- Luo, Z., G. Y. Liu, G. L. Stephens, and R. H. Johnson, 2009: Terminal versus transient cumulus congestus: A *CloudSat* perspective. *Geophys. Res. Lett.*, **36**, L05808, doi:10.1029/2008GL036927.
- Mace, G. G., R. Marchand, Q. Zhang, and G. Stephens, 2007: Global hydrometeor occurrence as observed by *CloudSat*: Initial observations from summer 2006. *Geophys. Res. Lett.*, **34**, L09808, doi:10.1029/2006GL029017.
- Malkus, J. S., 1952: The slopes of cumulus clouds in relation to external wind shear. *Quart. J. Roy. Meteor. Soc.*, **78**, 530–542, doi:10.1002/qj.49707833804.
- Manton, M. J., and W. R. Cotton, 1977: Parameterization of the atmospheric surface layer. *J. Atmos. Sci.*, **34**, 331–334, doi:10.1175/1520-0469(1977)034<0331:POTASL>2.0.CO;2.
- Marchand, R., G. G. Mace, T. Ackerman, and G. Stephens, 2008: Hydrometeor detection using *CloudSat*—An Earth-orbiting 94-GHz cloud radar. *J. Atmos. Oceanic Technol.*, **25**, 519–533, doi:10.1175/2007JTECHA1006.1.
- Medeiros, B., L. Nuijens, C. Antoniazzi, and B. Stevens, 2010: Low-latitude boundary layer clouds as seen by *CALIPSO*. *J. Geophys. Res.*, **115**, D23207, doi:10.1029/2010JD014437.
- Nuijens, L., B. Stevens, and A. P. Siebesma, 2009: The environment of precipitating shallow cumulus convection. *J. Atmos. Sci.*, **66**, 1962–1979, doi:10.1175/2008JAS2841.1.
- Pawlowska, H., and J.-L. Brenguier, 2003: An observational study of drizzle formation in stratocumulus clouds for general circulation model (GCM) parameterizations. *J. Geophys. Res.*, **108**, 8630, doi:10.1029/2002JD002679.
- Rapp, A. D., M. D. Lebsock, and T. S. L'Ecuyer, 2013: Low cloud precipitation climatology in the southeastern Pacific marine stratocumulus region using *CloudSat*. *Environ. Res. Lett.*, **8**, 014027, doi:10.1088/1748-9326/8/1/014027.
- Rauber, R. M., and Coauthors, 2007: Rain in shallow cumulus over the ocean: The RICO campaign. *Bull. Amer. Meteor. Soc.*, **88**, 1912–1928, doi:10.1175/BAMS-88-12-1912.
- Reiche, C. H., and S. Lasher-Trapp, 2010: The minor importance of giant aerosol to precipitation development within small trade wind cumuli observed during RICO. *Atmos. Res.*, **95**, 386–399, doi:10.1016/j.atmosres.2009.11.002.
- Rémillard, J., P. Kollias, E. Luke, and R. Wood, 2012: Marine boundary layer cloud observations in the Azores. *J. Climate*, **25**, 7381–7398, doi:10.1175/JCLI-D-11-00610.1.
- Saleeby, S. M., and W. R. Cotton, 2004: A large droplet mode and prognostic number concentration of cloud droplets in the Colorado State University Regional Atmospheric Modeling System (RAMS). Part I: Module descriptions and supercell test simulations. *J. Appl. Meteor.*, **43**, 182–195, doi:10.1175/1520-0450(2004)043<0182:ALMAPN>2.0.CO;2.
- , and S. C. van den Heever, 2013: Developments in the CSU-RAMS aerosol model: Emissions, nucleation, regeneration, deposition, and radiation. *J. Appl. Meteor. Climatol.*, **52**, 2601–2622, doi:10.1175/JAMC-D-12-0312.1.
- Satoh, M., T. Matsuno, H. Tomita, H. Miura, T. Nasuno, and S. Iga, 2008: Nonhydrostatic Icosahedral Atmospheric Model (NICAM) for global cloud resolving simulations. *J. Comput. Phys.*, **227**, 3486–3514, doi:10.1016/j.jcp.2007.02.006.
- Short, D. A., and K. Nakamura, 2000: TRMM radar observations of shallow precipitation over the tropical oceans. *J. Climate*, **13**, 4107–4124, doi:10.1175/1520-0442(2000)013<4107:TROOSP>2.0.CO;2.
- Snodgrass, E. R., L. Di Girolamo, and R. M. Rauber, 2009: Precipitation characteristics of trade wind clouds during RICO derived from radar, satellite, and aircraft measurements. *J. Appl. Meteor. Climatol.*, **48**, 464–483, doi:10.1175/2008JAMC1946.1.
- Stephens, G. L., and Coauthors, 2002: The *CloudSat* mission and the A-Train: A new dimension of space-based observations of clouds and precipitation. *Bull. Amer. Meteor. Soc.*, **83**, 1771–1790, doi:10.1175/BAMS-83-12-1771.
- , and Coauthors, 2008a: *CloudSat* mission: Performance and early science after the first year of operation. *J. Geophys. Res.*, **113**, D00A18, doi:10.1029/2008JD009982.
- , S. van den Heever, and L. Pakula, 2008b: Radiative–convective feedbacks in idealized states of radiative–convective equilibrium. *J. Atmos. Sci.*, **65**, 3899–3916, doi:10.1175/2008JAS2524.1.
- , and Coauthors, 2010: Dreary state of precipitation in global models. *J. Geophys. Res.*, **115**, D24211, doi:10.1029/2010JD014532.
- Storer, R. L., and S. C. van den Heever, 2013: Microphysical processes evident in aerosol forcing of tropical deep convective clouds. *J. Atmos. Sci.*, **70**, 430–446, doi:10.1175/JAS-D-12-076.1.
- Suzuki, K., G. Stephens, S. van den Heever, and T. Nakajima, 2011: Diagnosis of the warm rain process in cloud-resolving models using joint *CloudSat* and MODIS observations. *J. Atmos. Sci.*, **68**, 2655–2670, doi:10.1175/JAS-D-10-05026.1.
- Tomita, H., and M. Satoh, 2004: A new dynamical framework of nonhydrostatic global model using the icosahedral grid. *Fluid Dyn. Res.*, **34**, 357–400, doi:10.1016/j.fluidyn.2004.03.003.
- van den Heever, S. C., G. L. Stephens, and N. B. Wood, 2011: Aerosol indirect effects on tropical convection characteristics under conditions of radiative–convective equilibrium. *J. Atmos. Sci.*, **68**, 699–718, doi:10.1175/2010JAS3603.1.
- Webb, M. J., and Coauthors, 2006: On the contribution of local feedback mechanisms to the range of climate sensitivity in two GCM ensembles. *Climate Dyn.*, **27**, 17–38, doi:10.1007/s00382-006-0111-2.
- Witte, M. K., P. Y. Chuang, and G. Feingold, 2014: On clocks and clouds. *Atmos. Chem. Phys.*, **14**, 6729–6738, doi:10.5194/acp-14-6729-2014.
- Wood, R., 2012: Stratocumulus clouds. *Mon. Wea. Rev.*, **140**, 2373–2423, doi:10.1175/MWR-D-11-00121.1.
- Zuidema, P., E. R. Westwater, C. Fairall, and D. Hazen, 2005: Ship-based liquid water path estimates in marine stratocumulus. *J. Geophys. Res.*, **110**, D20206, doi:10.1029/2005JD005833.
- , and Coauthors, 2012: On trade wind cumulus cold pools. *J. Atmos. Sci.*, **69**, 258–280, doi:10.1175/JAS-D-11-0143.1.